Nano Energy 49 (2018) 515–522

Contents lists available at ScienceDirect

Nano Energy

journal homepage: www.elsevier.com/locate/nanoen

Full paper

Three-dimensional carbon framework anode improves sodiation–desodiation properties in ionic liquid electrolyte

Xu-Feng Luo[a], Ahmed S. Helal[b,e], Chien-Te Hsieh[c,d], Ju Li[b,*], Jeng-Kuei Chang[a,b,**]

[a] Institute of Materials Science and Engineering, National Central University, Taiwan
[b] Department of Nuclear Science and Engineering and Department of Materials Science and Engineering, Massachusetts Institute of Technology, 77 Massachusetts Avenue, Cambridge, MA 02139, USA
[c] Department of Mechanical, Aerospace and Biomedical Engineering, University of Tennessee, Knoxville, TN 37996, USA
[d] Department of Chemical Engineering and Materials Science, Yuan Ze University, Taiwan
[e] Nuclear Materials Authority, P. O. Box 540, El Maadi, Cairo, Egypt

ARTICLE INFO

Keywords:
Carbon framework
Three-dimensional electrode
Anodes
Ionic liquid
Sodium-ion batteries

ABSTRACT

Ionic liquid (IL), characterized by wide potential window, high thermal stability, negligible volatility, and low flammability, is a promising electrolyte for sodium-ion batteries (NIBs). However, the typical NIB anodes, such as hard carbon, show unsatisfactory capacities and poor charge–discharge rate capability in IL electrolyte at room temperature. A three-dimensional carbon framework (3-D CF) constructed with graphene nanosheets and carbon nanospheres is developed to address this issue. With this unique nano-architecture, the interfacial charge transfer, IL electrolyte infiltration, and Na^+ transport can be improved at room temperature. As a consequence, this electrode shows superior sodiation–desodiation properties, with a charge–discharge efficiency being stable over 250 cycles in *N*-propyl-*N*-methylpyrrolidinium bis(fluorosulfonyl)imide IL electrolyte. We also confirm that the 3-D CF electrode exhibits higher Coulombic efficiency and better cycling stability in the IL electrolyte than those found in conventional organic carbonate electrolyte, especially at an elevated temperature, due to the different chemistry of the solid–electrolyte interphase. The total heat releases of the sodiated 3-D CF samples contacted with IL and carbonate electrolytes, measured with differential scanning calorimetry up to 300 °C, are 250 and 805 J g^{-1}, respectively. The combination of the 3-D CF electrode and IL electrolyte shows great potential for NIB applications.

1. Introduction

Grid-scale energy storage is currently a bottleneck for low-carbon society [1,2]. Li-ion batteries (LIBs) widely used for consumer electronic devices and electric vehicles may not be an ideal candidate for this application, because of the relatively high cost and uneven distribution of Li in the Earth's crust [3,4]. It is noted that Li is also an important ingredient for the glass, ceramic, and the pharmaceutical industries, which are expected to grow at a rapid pace [5,6]. Na-ion batteries (NIBs) based on highly abundant Na are appealing alternatives or complements to LIBs. Recently, several favorable NIB cathodes, including polyanionic compounds, layered oxides, organic compounds, and Prussian blue analogues have been reported [7–9], with the performance being close to that of LIB cathodes [10]. Nevertheless, designing a good anode is challenging. For instance, the graphite anode (commonly used for LIBs) has poor Na^+ storage capability, due to the lack of stable graphite intercalation compounds for Na^+ [11,12]. While Ti-based anodes usually have low capacities, the alloying and conversion electrodes typically suffer from unsatisfactory reversibility and cyclic stability [13]. Development of a better anode material is thus urgently required, as it will be an enabling step for practical implementation of NIBs.

Organic electrolytes composed of Na salts and carbonate solvents are widely used in NIBs. However, the molecular organic solvent exhibits volatility and flammability, which can limit battery operation temperature and cause safety and environmental hazards [14,15]. The larger scale the energy storage system, the more severe these problems become. In this context, ionic liquid (IL) electrolytes, characterized by high thermal and chemical stability, large electrochemical stability window, negligible volatility, and fire-retardant ability, have received considerable attention [16]. The tunable physicochemical properties of ILs (by designing the cation/anion combinations) enable the possibility

* Corresponding author.
** Corresponding author at: Institute of Materials Science and Engineering, National Central University, 300 Jhong-Da Road, Taoyuan, Taiwan.
E-mail addresses: liju@mit.edu (J. Li), jkchang@ncu.edu.tw, jkchang@mit.edu (J.-K. Chang).

https://doi.org/10.1016/j.nanoen.2018.04.043
Received 16 January 2018; Received in revised form 26 February 2018; Accepted 15 April 2018
Available online 22 April 2018

of electrolyte optimization for various battery applications [17]. However, IL electrolytes typically have higher viscosity and lower conductivity at room temperature as compared to those of conventional organic electrolytes [15,18]. Many studies have thus focused on the use of IL electrolytes at elevated temperature, such as 90 °C, where the abovementioned limitations of ILs can be mitigated and organic electrolytes become unstable [19,20]. However, such a high temperature could complicate the system design and restrict the battery applications. At 25 °C, the hard carbon (HC) electrode, one of the most promising anodes for NIBs, exhibited a limited capacity of ~35 mAh g^{-1} (at a rate of 0.5 A g^{-1}) in IL electrolyte [21]. Clearly, a better electrode material and architecture are needed.

Graphene-based anodes have been proposed for conventional organic electrolyte NIBs. Owing to the unique two-dimensional structure with large surface area, high electron mobility, and great chemical stabilities, good charge storage performance has been reported for graphene anodes [22,23]. Heteroatom doping and KOH activation have been applied to graphene electrodes to enhance the electrochemical properties [24]. However, graphene anodes generally encounter two obstacles for practical applications. First, the highly anisotropic graphene sheets tend to restack during electrode preparation. The strong agglomeration can reduce reaction sites and hinder wetting and transport, limiting the electrode performance [25,26]. A three-dimensional carbon framework (3-D CF) electrode is thus developed in this study to deal with this difficulty. Second, the graphene sheets usually have a high surface area and high density of defective sites (non-perfect sp^2-hybridized carbon bonding produced during synthesis), which show high reactivity towards electrolytes [27,28]. Traditional organic electrolytes are unable to passivate the graphene anodes well, leading to distinct capacity fading upon electrode cycling [29,30]. The IL-derived solid–electrolyte interphase (SEI) is expected to stabilize the anode/electrolyte interface better [31,32]. Unfortunately, to date there have been no studies exploring the interaction between the graphene-based anode and IL electrolyte. This work thus aims to investigate this issue.

In the present study, a 3-D CF is constructed with graphene nanosheets (GNSs) and carbon nanospheres. Higher electrode performance (i.e., 235 mAh g^{-1} @0.03 A g^{-1} and 115 mAh g^{-1} @1 A g^{-1}) is achieved compared to that of HC, GNS, and many existing anodes in the literature for IL electrolytes at room temperature. Moreover, the SEI chemistry and charge–discharge properties of the 3-D CF electrodes in IL and conventional carbonate electrolytes are systematically examined. The thermal reactivity of the sodiated 3-D CF samples towards two electrolytes is measured using differential scanning calorimetry (DSC) to evaluate the safety properties with respect to thermal runaway in practical battery applications.

2. Experimental procedure

A modified Hummers method was used to chemically oxidize natural graphite [33,34]. The obtained graphite oxide (GO) was reduced and exfoliated to become GNSs via thermal treatment under H_2 gas at 400 °C. The carbon nanospheres were purchased from the Taiwan MAXWAVE Co. To prepare the 3-D CF, GNSs and carbon nanospheres (in a weight ratio of 7:3) were first sonicated in ethanol solution. Afterwards, the suspension was placed in a high-speed homogenizer (IKA, Model T25) equipped with a rotor-stator dispersing probe. The high velocity and narrow gap between the rotor and stator produced shear forces, collision, and cavitation, which resulted in effective dispersion. After homogenizing for 30 min at 2400 rpm under room temperature, the resulting 3-D CF was vacuum-dried at 100 °C for 12 h. For comparison, plain GNSs and commercial hard carbon (Carbotron P, Kureha Co.) were also studied in this work. The *N*-propyl-*N*-methylpyrrolidinium bis(fluorosulfonyl)imide (PMP–FSI) and *N*-propyl-*N*-methylpyrrolidinium bis(trifluoromethanesulfonyl)imide (PMP–TFSI) ILs purchased from Solvionic (99.5%) were vacuum-dried at 80 °C for 24 h before use. 1 M of NaFSI and NaTFSI salts (99.7 wt%, Solvionic) were respectively dissolved in above ILs to provide Na^+ conduction. A conventional organic electrolyte composed of 1 M $NaClO_4$ and ethylene carbonate (EC, 99 wt%, Alfa Aesar)/diethyl carbonate (DEC, 99 wt%, Alfa Aesar) co-solvent (1:1 by volume) was used for comparison.

The microstructures of the materials were examined using scanning electron microscopy (SEM; FEI Inspect F50) and transmission electron microscopy (TEM; JEOL 2100F). X-ray diffraction (XRD; Bruker D8 Advance with a Cu target) was used to characterize the crystallinity. The surface chemical compositions of the samples were analyzed with X-ray photoelectron spectroscopy (XPS; VG Sigma Probe). A Raman spectrometer (UniRAM Micro Raman; $\lambda = 532$ nm) was used to study the carbon bonding structures.

To prepare an electrode, a slurry consisting of 70 wt% active material powder, 20 wt% carbon black, and 10 wt% poly (vinylidene fluoride) in *N*-methyl-*2*-pyrrolidone solution was coated onto Cu foil. This active material ratio is for our academic research purpose and slightly lower than that of industrial practice. This electrode was vacuum-dried at 110 °C for 3 h, roll-pressed, and then punched to match the required dimensions of a CR2032 coin cell. The thickness of the coating layer was 20(± 2) μm. Thick Na foil and a glassy fiber membrane were used as the counter electrode and separator, respectively. The assembly of the coin cells was conducted in an argon-filled glove box (Innovation Technology Co. Ltd.), where both moisture and oxygen contents were maintained at below 0.5 ppm. Cyclic voltammetry (CV) was performed using a Biologic VSP-300 multi-channel potentiostat between 0.01 and 2.0 V at a potential sweep rate of 0.1 mV s^{-1}. The charge–discharge properties (such as capacity, rate capability, and cyclic stability) of various cells were evaluated using an Arbin BT-2043 battery tester at 25 °C unless otherwise specified. Electrochemical impedance spectroscopy (EIS) was conducted in a frequency range of 10 kHz–10 mHz and an AC amplitude of 10 mV.

The thermal reactivity of the sodiated 3-D CF samples towards IL and carbonate electrolytes was evaluated using DSC (Netzsch DSC3500) in the temperature range of 50–300 °C. The 3-D CF samples were presodiated to 0.01 V vs Na/Na^+, recovered from the coin cells, and then placed into Al capsules in the glove box without washing and drying. The samples were heated at a rate of 10 °C min^{-1} under a N_2 atmosphere.

3. Results and discussion

The morphologies of the GNSs and carbon nanospheres, examined using TEM, are shown in Fig. 1(a) and (b), respectively. The GNSs showed a flake-like structure with the lateral dimension of up to a micron. The high electron transparency reflected the thinness of the carbon sheet. An average particle diameter of ~40 nm was found for the carbon nanospheres. As shown in Fig. 1(c), after the homogenization process, the nanospheres are well dispersed on the GNSs. The nanospheres act as spacers between GNSs, not only preventing restacking of the carbon sheets but also creating a 3-D interpenetrating architecture. It is noted that this homogenization process is effective, facile, and can be easily scaled up for mass production.

The crystallinity of GNSs, carbon nanospheres, and 3-D CF were examined by XRD and shown in Fig. 2(a). The GNSs exhibited a major peak at 25.2°, which can be attributed to the (002) plane diffraction with a *d*-spacing of 0.354 nm (according to Bragg's law). The much smaller *d*-spacing than that of GO (~0.798 nm) indicates that the thermal treatment (400 °C in H_2) effectively reduced the sample. The nanospheres also showed a broad (002) peak with low diffraction intensity, which was ascribed to their nanocrystalline nature, as was observed by TEM. It was found that the 3-D CF sample showed an even broader (002) diffraction peak as compared to that of GNSs. This suggests that the number of carbon layers of GNSs was further reduced during the homogenization process. Fig. 2(b) shows the XPS data of various samples, with the C 1 s and O 1 s being the only signals observed, reflecting the high purity of the samples. The oxygen content of

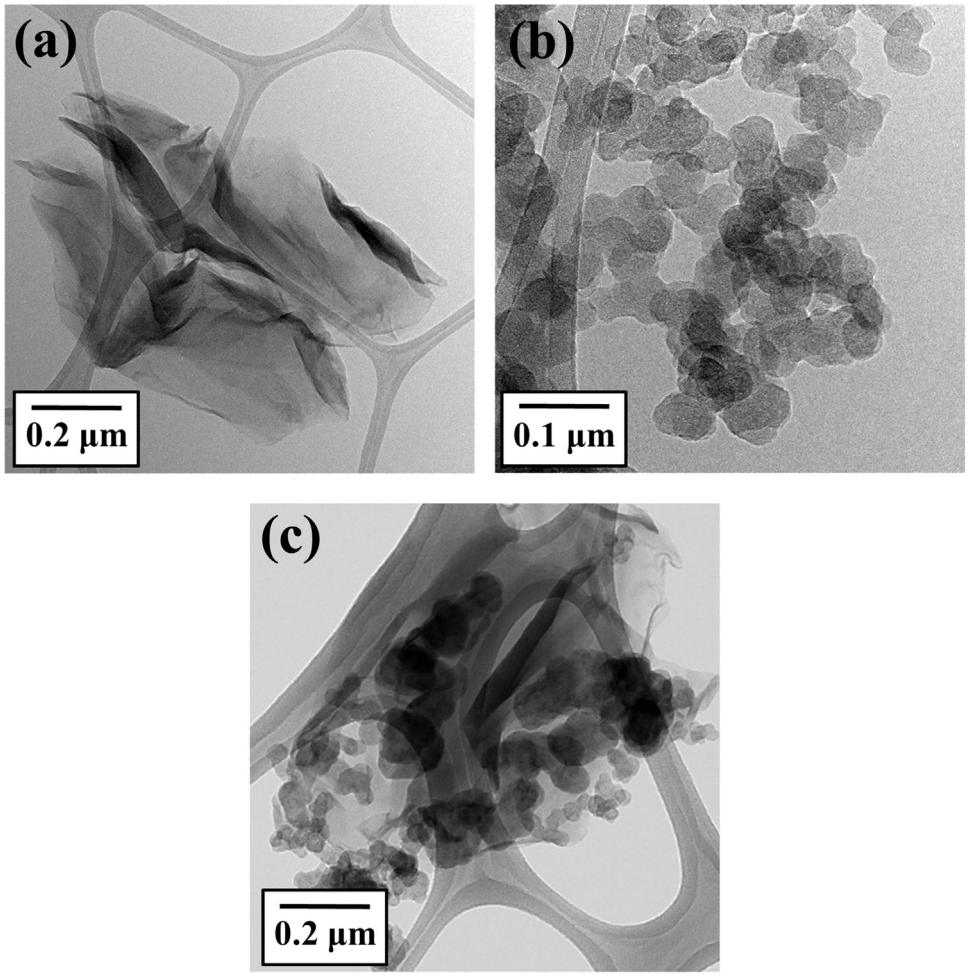

Fig. 1. TEM microstructures of (a) GNSs, (b) carbon nanospheres, and (c) 3-D CF.

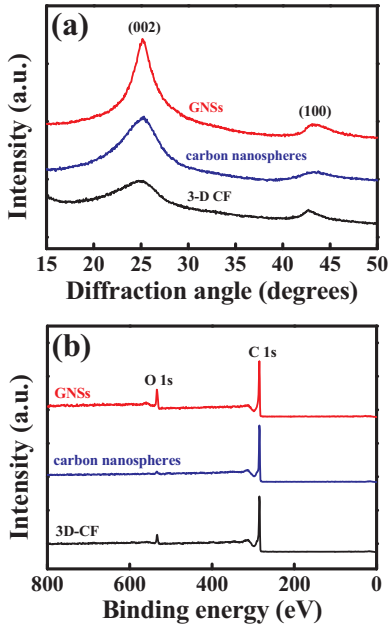

Fig. 2. (a) XRD patterns and (b) XPS spectra of GNSs, carbon nanospheres, and 3-D CF.

GNSs was attributed to the residual oxygen-containing functional groups. The high-resolution C 1s spectrum is shown in Fig. S1, which indicates the co-existence of C–O, C=O, and O=C–O groups on the GNS surface. These groups were found to facilitate reversible redox interactions with Na^+ during charging/discharging, contributing to pseudocapacitance [30,35,36]. The oxygen concentration for the 3-D CF sample was approximately 6 at%. Raman spectroscopy analyses were also conducted to examine the carbon bonding characteristics. As shown in Fig. S2, the D (~1340 cm^{-1}) and G (~1580 cm^{-1}) bands are recognized for all samples. The former is associated with imperfect carbon bonding, whereas the latter results from the Raman-allowed phonon vibration of a well-ordered sp^2 structure [37]. The D-to-G band intensity ratios for the GNSs, carbon nanospheres, and 3-D CF samples were found to be 1.08, 0.97, and 1.00, respectively.

CV measurements were conducted to characterize the electrochemical behavior of the electrodes in the PMP–FSI IL electrolyte. Fig. 3(a) and (b) show the initial five scans of the GNS and 3-D CF electrodes, which exhibit similar CV shapes. In the first negative scan, an irreversible cathodic peak appeared at ~0.6 V, which was associated with electrolyte decomposition and SEI formation [38,39]. The first-cycle coulombic efficiencies for the two electrodes were approximately 40%. From the second cycle on, the redox behavior of both electrodes became stable and highly reversible. Above 0.4 V, the nearly rectangular CV shape can be ascribed to the double-layer capacitance and reversible redox transitions of oxygen-containing functional groups on GNSs. Below 0.4 V, a distinct redox couple was observed, which was related to Na^+ insertion/desertion between the graphene layers [30,35]. It is found that the 3-D CF electrode shows a clearly larger

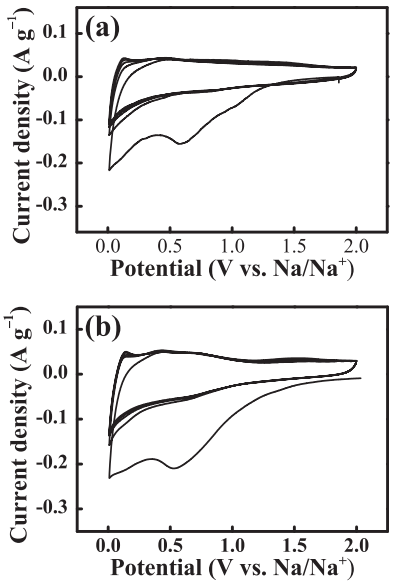

Fig. 3. Initial five CV scans of (a) GNS and (b) 3-D CF electrodes recorded at potential sweep rate of 0.1 mV s^{-1} in NaFSI/PMP–FSI IL electrolyte.

enclosed CV area, suggesting a higher charge storage capacity than that of the GNS electrode. This reveals that the 3-D architecture can effectively suppress graphene restacking and agglomeration, and thus maximize the active material utilization, resulting in superior electrochemical performance.

Fig. 4(a) and (b) show the charge–discharge curves of the GNS and 3-D CF electrodes recorded at various rates in the PMP–FSI IL electrolyte (after five conditioning cycles). At a current density of 0.03 A g^{-1}, the reversible capacities of the two electrodes were 165 and 235 mAh g^{-1}, respectively. The commercial HC (whose morphology and crystallinity are given in Fig. S3) electrode was subjected to a similar charge–discharge evaluation, and the data are shown in Fig. 4(c) for comparison. The voltage profile of the HC electrode is characterized by a sloping region (1.1–0.1 V), which is attributed to the Na^+ insertion between carbon layers, and a plateau region (below 0.1 V), which is associated with the filling of Na^+ into the HC micropores [40]. For the HC electrode, a capacity of 170 mAh g^{-1} was obtained at 0.03 A g^{-1} in the IL electrolyte. In the literature, an Sb/C composite showed a capacity of 80 mAh g^{-1} [41], an anatase TiO_2 showed a capacity of 150 mAh g^{-1} [42], a Nb-doped TiO_2 showed a capacity of 110 mAh g^{-1} [43], an organic quinone showed a capacity of 150 mAh g^{-1} [44], and a commercial HC showed a capacity of 170 mAh g^{-1} [21]. The nearly 40% improvement (235/170 = 1.382) shows that our 3-D CF, produced by a highly scalable synthesis route, is a promising NIB anode with IL electrolyte.

Fig. 4(d) compares the rate capability of the electrodes. At 1 A g^{-1}, the GNS, 3-D CF, and HC electrodes exhibited capacities of 85, 115, and 39 mAh g^{-1}, respectively. The traditional bulky electrode materials usually show limited charge–discharge kinetics in the IL electrolyte under room temperature, which has relatively high viscosity and low ion mobility (e.g., 27.4 cp and 2.0 mS cm^{-1} at 298 K for the PMP–FSI IL) [39]. The high-rate capability of the 3-D CF electrode (i.e., delivering a capacity of 115 mAh g^{-1} in 6.9 min (@1 A g^{-1})) clearly outperforms those of the reported NIB anodes in IL electrolytes, such as an anatase TiO_2 electrode (108 mAh g^{-1} @0.335 A g^{-1}) [42], a Nb-doped TiO_2 electrode (50 mAh g^{-1} @0.7 A g^{-1}) [43], an organic quinone electrode (100 mAh g^{-1} @0.3 A g^{-1}) [44], and a commercial HC electrode (35 mAh g^{-1} @0.5 A g^{-1}) [21].

EIS analyses were conducted to further characterize the electrode properties in the IL electrolyte. Two identical electrodes were pre-sodiated to 0.1 V vs. Na/Na^+ and then assembled as a symmetric cell, which can avoid the interference of large interfacial impedance at a Na electrode [32]. As shown in the Nyquist plot of Fig. 5(a), the spectra are composed of a semicircle (whose diameter represents the charge transfer resistance at the electrode interface) at high frequency, and a sloping line (which is associated with the Na^+ diffusion in the electrode) at low frequency [45]. The clearly larger charge transfer resistance at the HC electrode is attributed to the lower electrochemical surface area of HC due to its bulky nature, which limits the redox active sites in the electrolyte. The Bode plot in Fig. 5(b) indicates that the 3-D CF cell shows the lowest magnitude of total impedance among the cells in the whole frequency range. The open interpenetrating structure of 3-D CF (with suppressed graphene restacking) provides sufficient reaction sites to optimize the interfacial double-layer capacitance and pseudocapacitance. At the low-frequency region, the 3-D nanoarchitecture can ensure the electrolyte accessibility and shorten the Na^+ diffusion length in the electrode, leading to the lower impedance as compared to those of the GNS and HC electrodes. It is noted that the ion diffusion characteristic time constant (τ) in the electrode can be calculated as $\tau \approx l^2/D$, where l is the diffusion length and D is the diffusion coefficient [46]. The short l of the interpenetrating 3-D nanostructure is favorable for the high-rate charge–discharge performance.

It should be emphasized that, besides a gravimetric consideration, electrode volumetric performance is a crucial concern for practical battery applications. The compressed densities of the GNS, 3-D CF, and HC layers were measured to be 0.37, 0.5, and 0.625 g cm^{-3}, respectively. According to these values, the volumetric capacities of various electrodes in the IL electrolyte can be calculated, and the results are shown in Fig. 4(e). The 3-D CF electrode possesses volumetric capacities of 82 mAh cm^{-3} (at 0.03 A g^{-1}) and 40 mAh cm^{-3} (at 1 A g^{-1}), which are clearly higher than those of the GNS and HC electrodes. Nano-structured materials usually suffer from low tap density and therefore low volumetric performance. However, the experimental results confirm that the proposed 3-D CF electrode has a reasonable density and is able to show superior volumetric capacities than those of the HC electrode, especially at a high charge–discharge rate in the PMP–FSI IL electrolyte.

The 3-D CF electrode was also tested in 1 M NaTFSI/PMP–TFSI IL electrolyte, and the CV results are shown in Fig. S4. Interestingly, a much lower current density was found compared to that of Fig. 3(b). The similar IL, composed of the same pyrrolidinium cation and analogue imide anions (just $TFSI^-$ instead of FSI^-), resulted in totally different electrochemical behavior of the electrode. This highlights that the IL composition is very significant in determining the electrode Na^+ storage performance. It was reported that a HC electrode also showed a limited capacity in TFSI-based IL electrolyte [47]. Presumably, the decomposed TFSI forms an ion-resistive SEI that is unfavorable for Na^+ transport at room temperature. This SEI would hinder the electrode sodiation reaction, leading to the low redox activity. Since the exact mechanism is not yet clear, further investigation is required.

Fig. 6(a) shows the initial five CV scans of the 3-D CF electrode measured in conventional 1 M $NaClO_4$/EC:DEC organic electrolyte. A 1 M NaFSI/EC:DEC electrolyte has also been tested. However, as shown in Fig. S5, a large Al current collector corrosion current emerges at ~3.8 V, which prohibits this electrolyte from real applications. A commonly used salt for carbonate electrolytes in the literature, $NaClO_4$, is thus adopted. The electrochemical characteristics (Fig. 6(a)) resembled those found in the PMP–FSI IL electrolyte (Fig. 3(b)), suggesting a similar charge storage mechanism. Fig. S6 compares the initial five charge–discharge curves of the 3-D CF electrodes recorded in the organic carbonate and IL electrolytes at a rate of 0.03 A g^{-1}. The variations of coulombic efficiency (CE) with the cycle number are summarized in Table 1. The conventional carbonate electrolyte was not able to effectively passivate the electrode, with the CE value saturating at only ~95%, which was associated with unstable SEI. In contrast, the charge–discharge curves were well overlapping after three cycles and the CE reached almost 100% in the IL electrolyte. This suggests that the highly protective SEI that was formed can prevent continuous

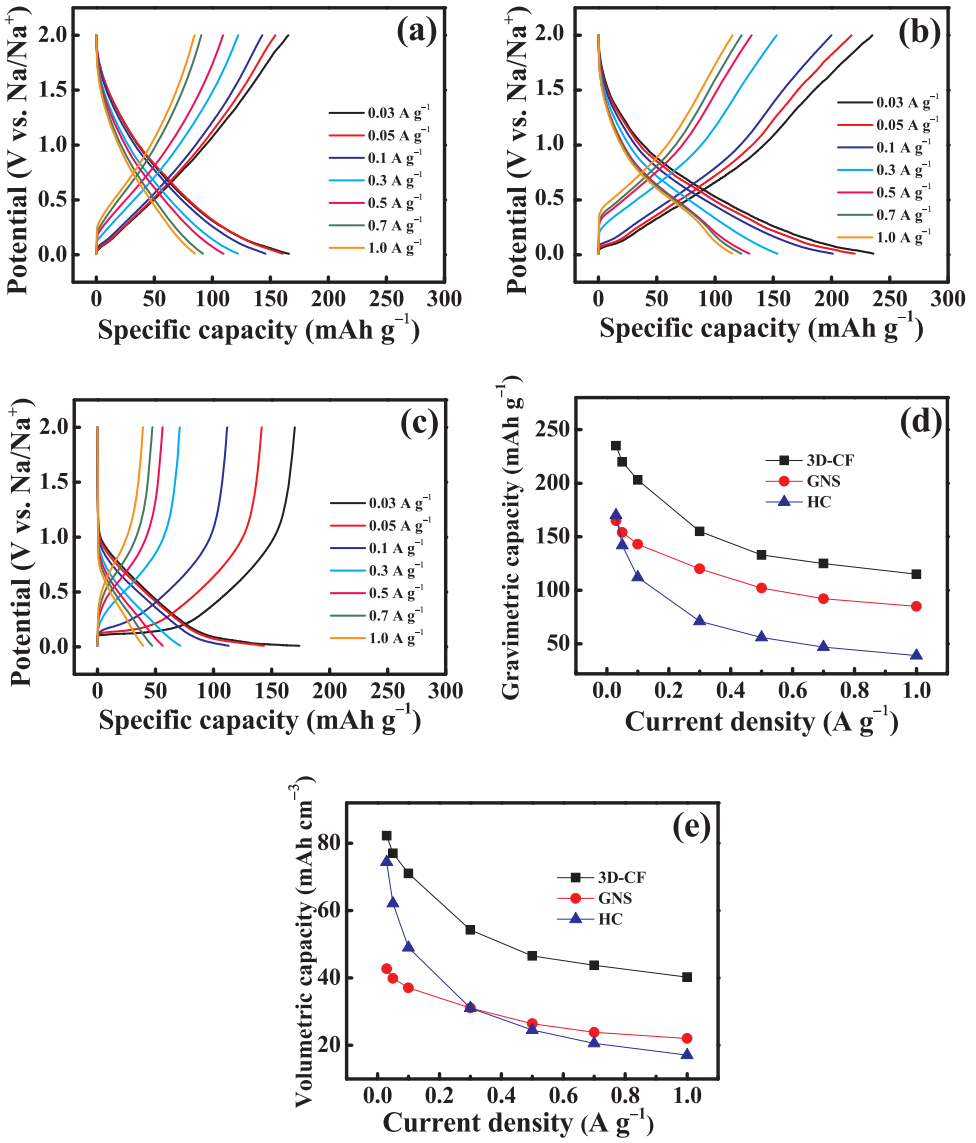

Fig. 4. Charge–discharge curves of (a) GNS, (b) 3-D CF, and (c) HC electrodes in NaFSI/PMP–FSI IL electrolyte. Comparisons of (d) gravimetric and (e) volumetric capacities of various electrodes recorded at various rates in NaFSI/PMP–FSI IL electrolyte.

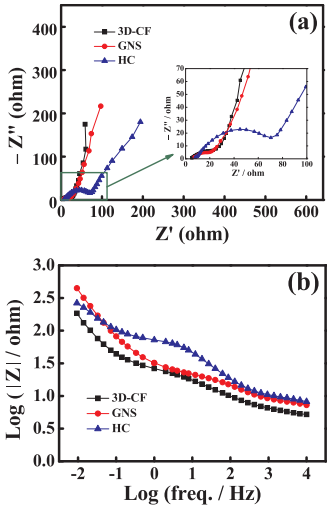

Fig. 5. EIS (a) Nyquist plots and (b) Bode plots for GNS, 3-D CF, and HC symmetric cells with NaFSI/PMP–FSI IL electrolyte.

decomposition of the electrolyte and ensure high reversibility of the electrode. Another advantage of the IL electrolyte is the higher anodic potential limit (> 5.5 V vs. Na/Na^+) than that (~4.7 V vs. Na/Na^+) of the conventional $NaClO_4$/EC:DEC electrolyte, as shown in Fig. S5.

Fig. 6(b) shows the electrode capacities measured in the organic carbonate electrolyte. Having relatively low viscosity and high conductivity (3.0 cp and 6.4 mS cm^{-1} at 298 K), this carbonate electrolyte typically enables higher capacities than those found in IL electrolyte. However, comparison of Fig. 6(b) to Fig. 4(d) indicates that the 3-D CF electrode can show similar performance in the two electrolytes. The other two materials exhibited a dramatic capacity reduction in the IL electrolyte. This confirms the uniqueness of the proposed 3-D CF architecture for use in the IL electrolyte. It is also noted in Fig. 6(b) that the benefit due to the nanosphere incorporation is less pronounced than that found in Fig. 4(d), implying that the GNS restacking problem is more serious in IL (probably due to the more difficult wetting and infiltration of IL that cause imbalances in capillary forces), which can be effectively minimized by introduction of the nanospheres.

XPS analyses were performed to characterize the chemistry of SEIs formed at the 3-D CF electrodes. Fig. 7(a) shows the survey scans of the electrodes after being cycled five times in the conventional carbonate

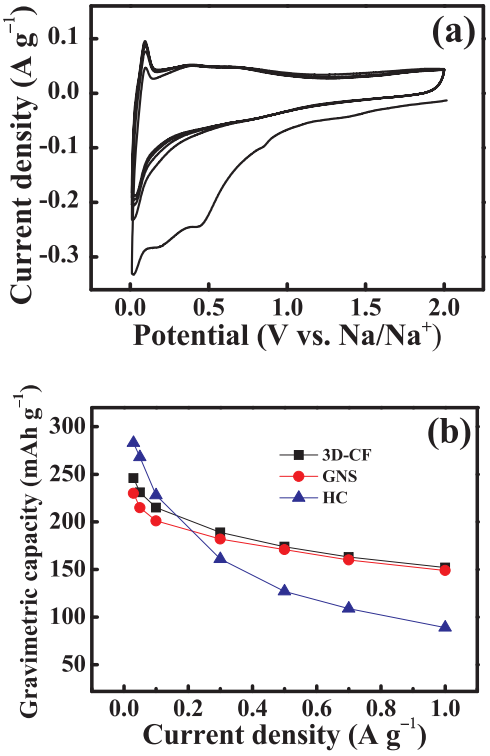

Fig. 6. (a) Initial five CV scans of 3-D CF electrode recorded at potential sweep rate of 0.1 mV s^{-1} in $NaClO_4$/EC:DEC electrolyte. (b) Comparison of gravimetric capacities of various electrodes recorded at various rates in $NaClO_4$/EC:DEC electrolyte.

Table 1
Variations of charge–discharge coulombic efficiency of 3-D CF electrodes cycled in two electrolytes at a current density of 0.03 A g^{-1} at 25 °C.

Electrolyte	1st cycle	2nd cycle	3rd cycle	4th cycle	5th cycle
$NaClO_4$/EC: DEC	40%	84%	90%	94%	95%
NaFSI/PMP–FSI	40%	96%	98%	100%	100%

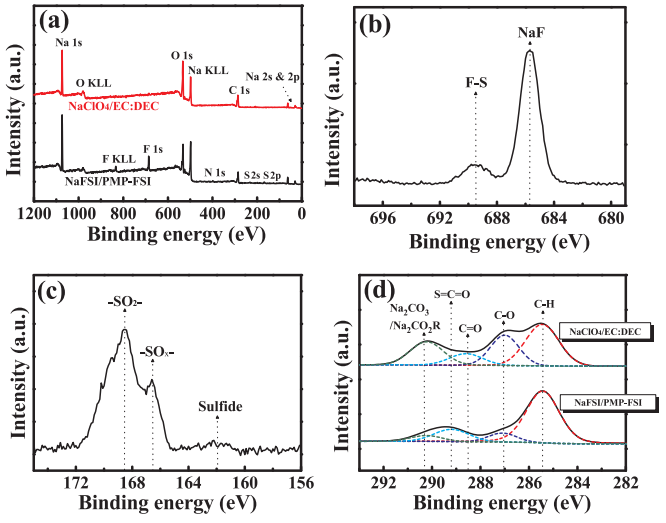

Fig. 7. (a) XPS survey scans of 3-D CF electrodes cycled in conventional carbonate and IL electrolytes. (b) F1s and (c) S2p spectra for electrode cycled in IL electrolyte. (d) Comparison of C 1s spectra of the two electrodes.

Table 2
XPS surface chemical composition (at%) of 3-D CF electrodes cycled in two electrolytes.

Electrolyte	C	O	F	Na	Cl	S	N
$NaClO_4$/EC: DEC	42	41	–	17	–	–	–
NaFSI/PMP–FSI	33	31	10	22	–	3	1

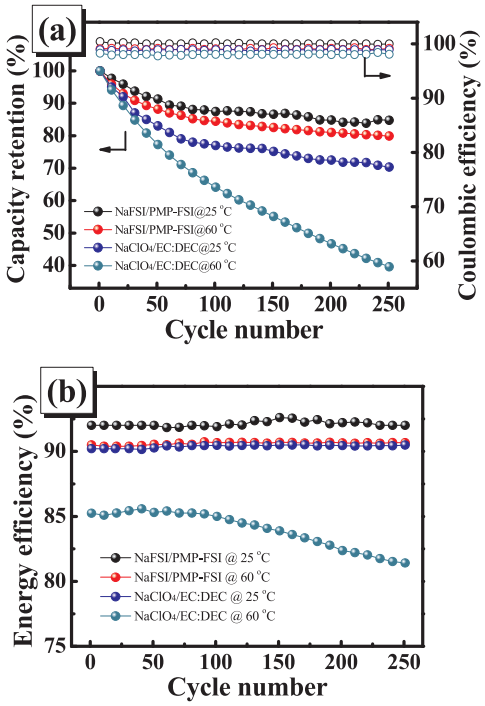

Fig. 8. Variations of (a) capacity and coulombic efficiency and (b) energy efficiency (a constant cathode potential of 3.8 V is assumed) versus cycle number for 3-D CF electrodes measured at 0.1 A g^{-1} in conventional carbonate and IL electrolytes at 25 and 60 °C.

and IL electrolytes. The chemical compositions of the two samples are summarized in Table 2. The conventional-electrolyte sample was enriched with C and O, which are thought to be the decomposition products of the carbonate solvent. The F and S signals found at the IL-electrolyte sample were further subjected to high-resolution scans, with the obtained data being shown in Fig. 7(b) and (c), respectively. The F 1 s spectrum exhibits a strong signal at ~685.7 eV related to NaF and a minor peak at ~689.4 eV associated with an F–S bond [48]. As for the sulfur spectrum, there are three constituents coexisting: -SO_2- (168.5 eV), SO_x (166.7 eV), and sulfide (162.1 eV) [49]. These species are associated with the solid reductive decomposition products of FSI^-. Fig. 7(d) compares the C 1 s spectra of the two electrodes. The conventional-electrolyte sample had relatively high contents of C–O, C=O, Na_2CO_3 and $NaCO_2R$, whereas the polyolefin ($(CH_2)_n$) and FSI-derived S=C=O were the dominant compounds for the IL-electrolyte sample. This IL anion-derived SEI is thought to be responsible for the superior CE and reversibility of the electrode.

Fig. 8(a) shows the cyclic stability of the 3-D CF electrodes (in terms of the capacity retention and CE variation during cycling) evaluated at a rate of 0.1 A g^{-1} at 25 and 60 °C (after five conditioning cycles). With the carbonate electrolyte, ~70% capacity retention was obtained at 25 °C after 250 charge–discharge cycles. When the temperature increased to 60 °C, the CE reduced to < 98%. Since the irreversible reaction between the electrode and electrolyte was promoted by the elevated temperature, a serious capacity decay was found (less than 40% of the initial capacity can be retained). In contrast, with better CE, the capacity retention ratios after the same number of cycles in the IL

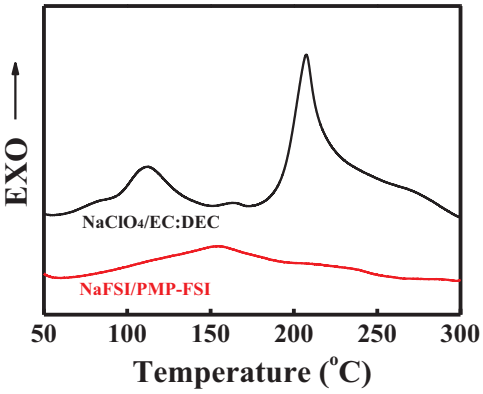

Fig. 9. DSC data of sodiated 3-D CF samples towards conventional carbonate and IL electrolytes.

electrolyte were 85% at 25 °C and 80% at 60 °C. This shows better high-temperature ageing performance of the IL cells, due to higher quality SEI formed with the reductive decomposition of FSI^- [50].

The energy efficiency variations upon cycling were further assessed to understand the resistance change of the 3-D CF electrodes. A constant cathode potential of 3.8 V is assumed in the calculation. The results in Fig. 8(b) show that the energy efficiency values of the IL-electrolyte cells, regardless of the temperature, keep stable above 90%, indicating little growth of the SEIs during the prolonged cycling. A clearly lower energy efficiency was found for the conventional-electrolyte cell at 60 °C. Moreover, the efficiency gradually decreased with increasing the cycle number. These results indicate a more ion-resistive SEI was formed, which was also unable to fully passivate the electrode and thus led to accumulation of the decomposition products over charging and discharging. The advantages of the IL electrolyte to enable superior electrode cyclability, especially at elevated temperatures, are remarkable.

In addition, the self-discharge tests for the 3-D CF electrode are performed both in the organic carbonate and IL electrolytes. Fig. S7 shows that after a rest of 5 days at 25 °C the capacity losses are 15% and 8%, respectively. The superior performance of the IL electrolyte should be associated with the interface SEI properties; however, more detailed investigations are needed.

The thermal reactivity of the electrolytes with the sodiated 3-D CF electrodes was evaluated using DSC, and the results are shown in Fig. 9. Two key parameters are major safety concerns with respect to thermal runaways: (i) the exothermic onset temperature, which is regarded as the initial step for thermal runaway, and (ii) the total heat generated, indicative of the magnitude of reactivity between the electrolyte and sodiated electrode [51]. As shown in the figure, the profile of the conventional-electrolyte sample can be distinguished into the following regions: the original SEI film breakdown at 70–95 °C, the chemical reaction between electrolyte and the SEI-free anode (leading to formation of a new SEI) at 95–140 °C, the thermal decomposition of this re-formed SEI at 150–170 °C, the bulk reaction between the electrolyte and sodiated electrode at 180–230 °C, and the interaction between the sodiated anode and the PVDF binder at 250 − 300 °C [52]. The exothermic onset temperature of ~70 °C and the measured total heat of ~805 J g^{-1} are close to those reported for HC with the same electrolyte [52]. In contrast, the IL-electrolyte sample did not show distinct DSC peaks, and only a broad hump with low exothermic intensity was observed. This indicates that the IL-derived SEI is robust and can withstand higher temperature. Moreover, the high chemical stability of IL towards the reducing sodiated anode also contributed to the low thermal reactivity. The total heat generated was as low as ~250 J g^{-1}, reflecting the much improved safety characteristics.

To demonstrate the effectiveness of the new anode and IL electrolyte, full-cell cycling is needed. A $Na_3V_2(PO_4)_3$//NaFSI/PMP–FSI//3-D CF full cell has been constructed, with cathode/anode capacity ratio of 1/1.2 at 1 C (this ratio decreases with increasing C rate). The charge–discharge data are shown in Fig. S8. Although further optimization of the full cell is needed, the results have confirmed that a full-cell NIB involving the proposed anode and electrolyte is feasible.

4. Conclusions

A facile and scalable synthesis method was developed to fabricate 3-D CF, consisting of graphene nanosheets interpenetrating with carbon nanospheres, with decent compressed density. This architecture facilitates the interfacial charge transfer reaction, promotes electrolyte accessibility, and shortens the Na^+ diffusion length in the electrode. The electrode showed excellent charge − discharge capacities in PMP − FSI IL electrolyte, being 235 mAh g^{-1} @ 0.03 A g^{-1} and 115 mAh g^{-1} @ 1 A g^{-1} at 25 °C with great cycling stability. The rate capability and volumetric performance of the 3-D CF electrode are superior to those of a commercial HC electrode. The IL-derived SEI, which involved the reductive decomposition products of FSI^-, was found to be more robust than the carbonate-electrolyte-derived SEI, resulting in the higher CE and better cyclability of the electrode, especially with elevated-temperature operations. The thermal reactivity of the sodiated 3-D CF electrode towards the PMP − FSI electrolyte was much lower than that towards the conventional carbonate electrolyte. Integrating the proposed 3-D CF electrode with IL electrolyte is a unique combination that shows great potential for high-performance, high-durability, and safe NIB applications.

Acknowledgements

The financial support provided for this work by the Ministry of Science and Technology (MOST) of Taiwan (Grant No. 106-2628-E-008-002-MY3 and 106-2221-E-008-091-MY3) is gratefully appreciated. JL acknowledges support by NSF ECCS-1610806.

Appendix A. Supporting information

Supplementary data associated with this article can be found in the online version at http://dx.doi.org/10.1016/j.nanoen.2018.04.043.

References

[1] B. Dunn, H. Kamath, J.M. Tarascon, Electrical energy storage for the grid: a battery of choices, Science 334 (2011) 928–935.
[2] J. Liu, J.G. Zhang, Z. Yang, J.P. Lemmon, C. Imhoff, G.L. Graff, L. Li, J. Hu, C. Wang, J. Xiao, G. Xia, V.V. Viswanathan, S. Baskaran, V. Sprenkle, X. Li, Y. Shao, B. Schwenzer, Materials science and materials chemistry for large scale electrochemical energy storage: from transportation to electrical grid, Adv. Funct. Mater. 23 (2013) 929–946.
[3] N. Yabuuchi, K. Kubota, M. Dahbi, S. Komaba, Research development on sodium-ion batteries, Chem. Rev. 114 (2014) 11636–11682.
[4] L.P. Wang, L. Yu, X. Wang, M. Srinivasan, Z.J. Xu, Recent developments in electrode materials for sodium-ion batteries, J. Mater. Chem. A 3 (2015) 9353–9378.
[5] H. Pan, Y.S. Hu, L. Chen, Room-temperature stationary sodium-ion batteries for large-scale electric energy storage, Energy Environ. Sci. 6 (2013) 2338.
[6] M.D. Slater, D. Kim, E. Lee, C.S. Johnson, Sodium-Ion batteries, Adv. Funct. Mater. 23 (2013) 947–958.
[7] D. Kundu, E. Talaie, V. Duffort, L.F. Nazar, The emerging chemistry of sodium ion batteries for electrochemical energy storage, Angew. Chem. Int. Ed. 54 (2015) 3431–3448.
[8] V. Palómares, M. Casas-Cabanas, E. Castillo-Martínez, M.H. Han, T. Rojo, Update on Na-based battery materials. A growing research path, Energy Environ. Sci. 6 (2013) 2312–2337.
[9] M.H. Han, E. Gonzalo, G. Singh, T. Rojo, A comprehensive review of sodium layered oxides: powerful cathodes for Na-ion batteries, Energy Environ. Sci. 8 (2015) 81–102.
[10] V. Palómares, P. Serras, I. Villaluenga, K.B. Hueso, J. Carretero-González, T. Rojo, Na-ion batteries, recent advances and present challenges to become low cost energy storage systems, Energy Environ. Sci. 5 (2012) 5884.
[11] Y. Cao, L. Xiao, M.L. Sushko, W. Wang, B. Schwenzer, J. Xiao, Z. Nie, L.V. Saraf, Z. Yang, J. Liu, Sodium ion insertion in hollow carbon nanowires for battery applications, Nano Lett. 12 (2012) 3783–3787.
[12] X.F. Luo, C.H. Yang, Y.Y. Peng, N.W. Pu, M.D. Ger, C.T. Hsieh, J.K. Chang,

Graphene nanosheets, carbon nanotubes, graphite, and activated carbon as anode materials for sodium-ion batteries, J. Mater. Chem. A 3 (2015) 10320–10326.
[13] H. Kang, Y. Liu, K. Cao, Y. Zhao, L. Jiao, Y. Wang, H. Yuan, Update on anode materials for Na-ion batteries, J. Mater. Chem. A 3 (2015) 17899–17913.
[14] A. Ponrouch, D. Monti, A. Boschin, B. Steen, P. Johansson, M.R. Palacín, Non-aqueous electrolytes for sodium-ion batteries, J. Mater. Chem. A 3 (2015) 22–42.
[15] K. Vignarooban, R. Kushagra, A. Elango, P. Badami, B.E. Mellander, X. Xu, T.G. Tucker, C. Nam, A.M. Kannan, Current trends and future challenges of electrolytes for sodium-ion batteries, Int. J. Hydrog. Energy 41 (2016) 2829–2846.
[16] M. Watanabe, M.L. Thomas, S. Zhang, K. Ueno, T. Yasuda, K. Dokko, Application of ionic liquids to energy storage and conversion materials and devices, Chem. Rev. 117 (2017) 7190–7239.
[17] R. Hagiwara, J.S. Lee, Ionic liquids for electrochemical devices, Electrochemistry 75 (2007) 23–34.
[18] H. Che, S. Chen, Y. Xie, H. Wang, K. Amine, X.Z. Liao, Z.F. Ma, Electrolyte design strategies and research progress for room-temperature sodium-ion batteries, Energy Environ. Sci. 10 (2017) 1075–1101.
[19] M. Forsyth, H. Yoon, F. Chen, H. Zhu, D.R. MacFarlane, M. Armand, P.C. Howlett, Novel Na^+ ion diffusion mechanism in mixed organic–inorganic ionic liquid electrolyte leading to high Na^+ transference number and stable, high rate electrochemical cycling of sodium cells, J. Phys. Chem. C 120 (2016) 4276–4286.
[20] K. Matsumoto, Y. Okamoto, T. Nohira, R. Hagiwara, Thermal and transport properties of $Na[N(SO_2F)_2]$–[N-Methyl-N-propylpyrrolidinium][$N(SO_2F)_2$] ionic liquids for Na secondary batteries, J. Phys. Chem. C 119 (2015) 7648–7655.
[21] C. Ding, T. Nohira, R. Hagiwara, A. Fukunaga, S. Sakai, K. Nitta, Electrochemical performance of hard carbon negative electrodes for ionic liquid-based sodium ion batteries over a wide temperature range, Electrochim. Acta 176 (2015) 344–349.
[22] A.K. Geim, K.S. Novoselov, The rise of graphene, Nat. Mater. 6 (2007) 183–191.
[23] R. Raccichini, A. Varzi, S. Passerini, B. Scrosati, The role of graphene for electrochemical energy storage, Nat. Mater. 14 (2015) 271–279.
[24] C. Xu, B. Xu, Y. Gu, Z. Xiong, J. Sun, X.S. Zhao, Graphene-based electrodes for electrochemical energy storage, Energy Environ. Sci. 6 (2013) 1388.
[25] H.R. Byon, B.M. Gallant, S.W. Lee, Y. Shao-Horn, Role of oxygen functional groups in carbon nanotube/graphene freestanding electrodes for high performance lithium batteries, Adv. Funct. Mater. 23 (2013) 1037–1045.
[26] Y.S. Yun, Y.U. Park, S.J. Chang, B.H. Kim, J. Choi, J. Wang, D. Zhang, P.V. Braun, H.J. Jin, K. Kang, Crumpled graphene paper for high power sodium battery anode, Carbon 99 (2016) 658–664.
[27] K.P. Loh, Q. Bao, G. Eda, M. Chhowalla, Graphene oxide as a chemically tunable platform for optical applications, Nat. Chem. 2 (2010) 1015–1024.
[28] P.A. Denis, F. Iribarne, Comparative study of defect reactivity in graphene, J. Phys. Chem. C 117 (2013) 19048–19055.
[29] J. Zhang, D.W. Wang, W. Lv, S. Zhang, Q. Liang, D. Zheng, F. Kang, Q.H. Yang, Achieving superb sodium storage performance on carbon anodes through an ether-derived solid electrolyte interphase, Energy Environ. Sci. 10 (2017) 370–376.
[30] X.F. Luo, S.Y. Wang, C.M. Tseng, S.W. Lee, W.H. Chiang, J.K. Chang, Microplasma-assisted bottom-up synthesis of graphene nanosheets with superior sodium-ion storage performance, J. Mater. Chem. A 4 (2016) 7624–7631.
[31] M. Dahbi, M. Fukunishi, T. Horiba, N. Yabuuchi, S. Yasuno, S. Komaba, High performance red phosphorus electrode in ionic liquid-based electrolyte for Na-ion batteries, J. Power Sources 363 (2017) 404–412.
[32] C.H. Wang, C.H. Yang, J.K. Chang, Suitability of ionic liquid electrolytes for room-temperature sodium-ion battery applications, Chem. Commun. 52 (2016) 10890–10893.
[33] C.T. Hsieh, Y.F. Chen, C.E. Lee, Y.M. Chiang, H. Teng, Thermal transport in stereo carbon framework using graphite nanospheres and graphene nanosheets, Carbon 106 (2016) 132–141.
[34] H.L. Poh, F. Šaněk, A. Ambrosi, G. Zhao, Z. Sofer, M. Pumera, Graphenes prepared by staudenmaier, hofmann and hummers methods with consequent thermal exfoliation exhibit very different electrochemical properties, Nanoscale 4 (2012) 3515–3522.
[35] X.F. Luo, C.H. Yang, J.K. Chang, Correlations between electrochemical Na^+ storage properties and physiochemical characteristics of holey graphene nanosheets, J. Mater. Chem. A 3 (2015) 17282–17289.
[36] Y. Shao, J. Xiao, W. Wang, M. Engelhard, X. Chen, Z. Nie, M. Gu, L.V. Saraf, G. Exarhos, J.G. Zhang, J. Liu, Surface-driven sodium ion energy storage in nanocellular carbon foams, Nano Lett. 13 (2013) 3909–3914.
[37] A. Jorio, M.S. Dresselhaus, R. Saito, G. Dresselhaus, Raman Spectroscopy in Graphene Related Systems, WILEY-VCH, 2011.
[38] H.C. Chen, J. Patra, S.W. Lee, C.J. Tseng, T.Y. Wu, M.H. Lin, J.K. Chang, Electrochemical Na^+ storage properties of SnO_2/graphene anodes in carbonate-based and ionic liquid electrolytes, J. Mater. Chem. A 5 (2017) 13776–13784.
[39] C.Y. Li, J. Patra, C.H. Yang, C.M. Tseng, S.B. Majumder, Q.F. Dong, J.K. Chang, Electrolyte optimization for enhancing electrochemical performance of antimony sulfide/graphene anodes for sodium-ion batteries–carbonate-based and ionic liquid electrolytes, ACS Sustain. Chem. Eng. 5 (2017) 8269–8276.
[40] S. Komaba, W. Murata, T. Ishikawa, N. Yabuuchi, T. Ozeki, T. Nakayama, A. Ogata, K. Gotoh, K. Fujiwara, Electrochemical na insertion and solid electrolyte interphase for hard-carbon electrodes and application to Na-ion batteries, Adv. Funct. Mater. 21 (2011) 3859–3867.
[41] I. Hasa, S. Passerini, J. Hassoun, Characteristics of an ionic liquid electrolyte for sodium-ion batteries, J. Power Sources 303 (2016) 203–207.
[42] L. Wu, A. Moretti, D. Buchholz, S. Passerini, D. Bresser, Combining ionic liquid-based electrolytes and nanostructured anatase TiO_2 anodes for intrinsically safer sodium-ion batteries, Electrochim. Acta 203 (2016) 109–116.
[43] H. Usui, Y. Domi, M. Shimizu, A. Imoto, K. Yamaguchi, H. Sakaguchi, Niobium-doped titanium oxide anode and ionic liquid electrolyte for a safe sodium-ion battery, J. Power Sources 329 (2016) 428–431.
[44] B.E. Gurkan, Z. Qiang, Y.M. Chen, Y. Zhu, B.D. Vogt, Enhanced cycle performance of quinone-based anodes for sodium ion batteries by attachment to ordered mesoporous carbon and use of ionic liquid electrolyte, J. Electrochem. Soc. 164 (2017) H5093–H5099.
[45] J. Patra, H.C. Chen, C.H. Yang, C.T. Hsieh, C.Y. Su, J.K. Chang, High dispersion of 1-nm SnO_2 particles between graphene nanosheets constructed using supercritical CO_2 fluid for sodium-ion battery anodes, Nano Energy 28 (2016) 124–134.
[46] Y. Wang, H. Li, P. He, E. Hosono, H. Zhou, Nano active materials for lithium-ion batteries, Nanoscale 2 (2010) 1294–1305.
[47] M. Egashira, T. Tanaka, N. Yoshimoto, M. Morita, Influence of ionic liquid species in non-aqueous electrolyte on sodium insertion into hard carbon, Electrochemistry 80 (2012) 755–758.
[48] K. Takada, Y. Yamada, E. Watanabe, J. Wang, K. Sodeyama, Y. Tateyama, K. Hirata, T. Kawase, A. Yamada, Unusual passivation ability of superconcentrated electrolytes toward hard carbon negative electrodes in sodium-ion batteries, ACS Appl. Mater. Interfaces 9 (2017) 33802–33809.
[49] Y. Yamada, A. Yamada, Superconcentrated electrolytes to create new interfacial chemistry in non-aqueous and aqueous rechargeable batteries, Chem. Lett. 46 (2017) 1056–1064.
[50] L. Suo, W. Xue, M. Gobet, S.G. Greenbaum, C. Wang, Y. Chen, W. Yang, Y. Li, Ju Li, Fluorine-donating electrolytes enable highly reversible 5-V-class Li metal batteries, PNSA, ⟨http://dx.doi.org/10.1073/pnas.1712895115⟩.
[51] G.G. Eshetu, S. Grugeon, H. Kim, S. Jeong, L. Wu, G. Gachot, S. Laruelle, M. Armand, S. Passerini, Comprehensive insights into the reactivity of electrolytes based on sodium ions, ChemSusChem 9 (2016) 462–471.
[52] A. Ponrouch, E. Marchante, M. Courty, J.M. Tarascon, M.R. Palacín, In search of an optimized electrolyte for Na-ion batteries, Energy Environ. Sci. 5 (2012) 8572.